

The dynamics of conformational isomerization in flexible biomolecules. II. Simulating isomerizations in a supersonic free jet with master equation dynamics

David A. Evans^{a)} and David J. Wales

University Chemical Laboratories, Lensfield Road, Cambridge, CB2 1EW, United Kingdom

Brian C. Dian and Timothy S. Zwier

Department of Chemistry, 560 Oval Drive, Purdue University, West Lafayette, Indiana 47907-2084

(Received 7 August 2003; accepted 26 September 2003)

Infrared-induced conformational isomerization of N-acetyl-tryptophan methyl amide is studied theoretically using a microcanonical Rice–Ramsperger–Kassel–Marcus description of the rates on potential energy surfaces calculated using the AMBER and OPLS-AA force fields. The results are compared with the experimental data from Dian *et al.* in the preceding paper [J. Chem. Phys. **120**, 133 (2004)]. An exhaustive search of the potential energy surfaces locates all minima and transition states on these surfaces. A simple model is proposed for the vibrational cooling, and an appropriate cooling rate is chosen as the standard conditions for the master equation simulations by comparison with experiment. The two potential energy surfaces differ in the relative energies of minima and the heights of key transition states, leading to differences in the dominant pathways and rates of conformational isomerization. The predicted quantum yields depend sensitively on the cooling rate, varying from the slow cooling limit in which equilibrium populations are achieved to the fast quenching limit in which conformational isomerization is shut off. The excitation energy is varied from 5 to 20 kcal mol⁻¹. At the lowest energies, isomerization is completely quenched, while at the highest energies, equilibrium conditions are achieved. In between these extremes, the quantum yields are sensitive to the excitation energy, and can be used to locate the rate-limiting barriers to isomerization. © 2004 American Institute of Physics. [DOI: 10.1063/1.1626541]

I. INTRODUCTION

The preceding paper (Ref. 1) presented a description of the experimental methods used to study the IR-induced conformational isomerization dynamics in isolated flexible biomolecules following selective excitation of single conformations in their hydride stretch fundamentals. The methods of IR-UV hole-filling spectroscopy and IR-induced population transfer spectroscopy determine which products are formed, and in what abundance. By carrying out the IR excitation early in a supersonic expansion, cooling collisions have collected the population into the zero-point levels of the product conformational wells prior to interrogation of the final product populations.

These methods were first applied to two methyl capped dipeptides, N-acetyl tryptophan methyl amide (NATMA) and N-acetyl tryptophan amide. These molecules are large enough to possess several flexible sites that make them conformationally complex, but small enough that their potential energy surfaces (PESs) can still be characterized and probed in some detail. The major results of the experimental work were sets of isomerization quantum yields following excitation of each of the unique amide NH stretch fundamentals of these molecules.¹

Molecular conformational changes can be described theoretically in terms of transitions between local minima on

the PES, which represent the stable conformers. These transitions are mediated by transition states, defined as stationary points of the PES with one negative eigenvalue.² Even small molecules can have relatively complex networks of connections between stable conformers and, in order to understand the overall kinetics of such systems, it is essential to be able to map the topology and barrier distributions of these pathways.^{3,4}

If the vibrational energy per degree of freedom of a system is low compared to the barrier height for a given rearrangement pathway, then it is generally assumed that the rate can be described by a statistical theory, such as the Rice–Ramsperger–Kassel–Marcus (RRKM) model,⁵ where energy is assumed to be equilibrated over all modes of a particular conformer. Vibrational spectroscopy naturally involves the excitation of a single mode of a molecule, and so the degree of applicability of statistical rate theories depends on the extent and rate of intramolecular vibrational relaxation. The experiments on NATMA show relatively little variation in the quantum yields when different modes of the same conformer are excited, but differing isomerization patterns when different conformers are excited, indicating that a statistical rate theory may be sufficient, provided the topology of the landscape is known.

The present theoretical study seeks to model the experimental results on NATMA. A description of the low-energy region of the PES is provided using two empirical force fields. This allows an analysis of the dominant isomerization

^{a)}Electronic mail: dae22@cam.ac.uk

pathways within a microcanonical RRKM description of the rates, and hence predictions for the time scale of isomerization events. The rate of cooling within the expanding supersonic free jet will clearly affect the reaction rates and product quantum yields, and so we develop a simple model for the collisional quenching of vibrational energy, and examine the effect of differing initial energies and cooling rates on the quantum yields following IR excitation.

II. LANDSCAPE SEARCHING AND REPRESENTATION

The NATMA molecule was represented by two alternative all-atom empirical force fields, AMBER⁶ (using the parm96.dat parameters)⁷ and OPLS-AA.⁸ The first stage in describing the system for each force field was to construct a database of minima and transition states connected via steepest-descent paths, using a parallelized landscape searching algorithm.^{9,10} Minima and transition states were located using eigenvector-following with a separate Lagrange multiplier for each eigenvector and the trust radius scheme for selecting step sizes.^{11,12} All stationary points were converged to a root-mean-squared gradient of less than 10^{-6} kcal mol⁻¹ Å⁻¹. In brief, the search algorithm involves starting from a minimum in the database (initially, just a single low-energy minimum) and perturbing the geometry by stepping 0.1 Å along the eigenvector corresponding to the lowest Hessian eigenvalue not already searched, then performing a transition state search. If the transition state search converges, then the two minima that it connects are found by minimization after stepping off 0.05 Å in either direction along the eigenvector corresponding to the negative Hessian eigenvalue (the reactive mode). If one of these two minima is in the database, then the other minimum and transition state are added to the database, and the algorithm proceeds from the lowest-energy minimum in the database with unsearched eigenvectors.

This search resulted in databases of 164 minima and 714 transition states for AMBER, and 178 minima and 836 transition states for OPLS-AA. The best way to visualize such databases is with disconnectivity graphs, which partition the minima into disjoint sets based on the energies of connecting transition states.¹³ A disconnectivity graph of NATMA for OPLS-AA is shown in Fig. 1. The graph is split into four main branches, corresponding to the four possible *cis/trans* peptide bond isomers. The most significant part of the landscape is the lowest energy all-*trans* region. The three lowest-energy minima found with both force fields correspond to the conformers that were predicted to be the most important in the experimental work,^{1,14,15} and are labeled A, B, and C according to the notation of Ref. 1. All the minima in the branch of the graph within which these three minima are connected are replotted in Figs. 2 and 3.

For the majority of significant minima, it was possible to unambiguously match structures found in the two force fields, based on the root-mean-square displacement of their atomic coordinates. Nodes corresponding to these minima are labeled with capital letters, starting with experimentally observed conformers A, B, and C as previously discussed and proceeding alphabetically in ascending energy order ac-

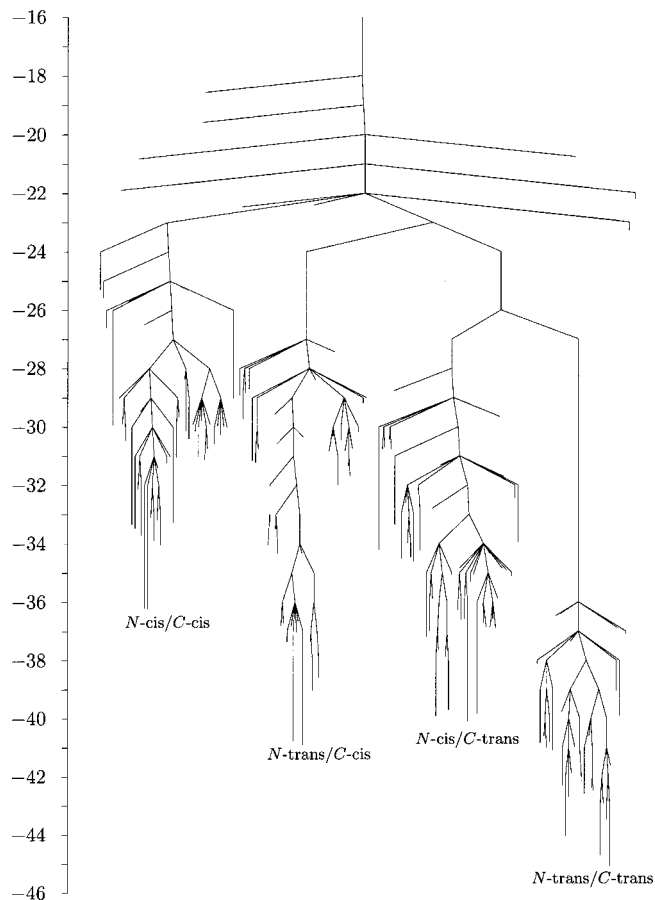


FIG. 1. Disconnectivity graph for the NATMA molecule calculated using the OPLS-AA force field. The branches are labeled according to the orientation of the peptide bonds at the N and C ends of the amino acid. The energy is in units of kcal mol⁻¹.

ording to the AMBER force field. Minima found in the OPLS-AA force field but not in AMBER are labeled in Fig. 3 with lower case letters.

While both force fields agree with the experimental finding that there are three dominant conformers, they differ in their prediction of the relative energy ordering. OPLS-AA has $B < A < C$ and AMBER has $A < B < C$. This difference will clearly affect the predictions of the occupation probability. The experimental observation has $P_B > P_C > P_A$, which is not in exact agreement with either force field if potential energy alone dictates the relative populations of the conformers. In reality, the populations downstream in the expansion depend on the relative energies of the minima and on the kinetics of cooling in the expansion. We will return to this point in Sec. V.

Further differences between the potentials can be seen in the barriers between the different conformers. For OPLS-AA, the disconnectivity graph shows that the barrier separating minimum C from the global minimum B is much higher than the corresponding barrier between A and B. In contrast, for AMBER, the three lowest-energy minima are all separated by barriers of similar size (5.5 kcal mol⁻¹), with minima C and B separated by a slightly smaller barrier than A and B. The size of the barriers has consequences for the relaxation dynamics of the system, as described in Sec. VI.

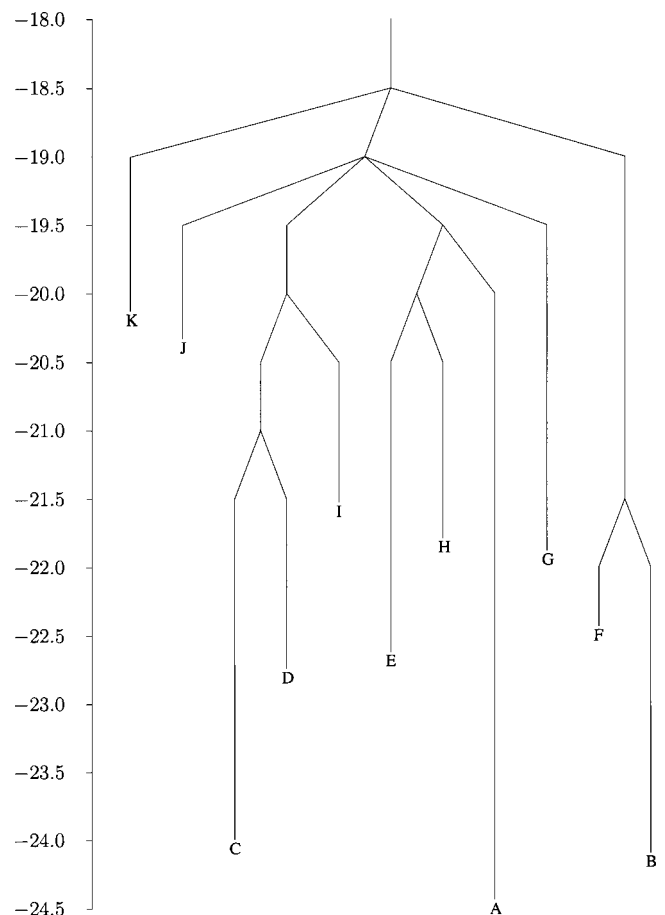


FIG. 2. Disconnectivity graph for the all-*trans* peptide bond region of NATMA calculated using the AMBER force field. The energy is in units of kcal mol⁻¹.

III. THERMODYNAMICS AND KINETICS

If the normal mode frequencies of the minima and transition states are known along with their potential energies, it is possible to estimate the partition functions for each minimum and transition state, and hence the equilibrium occupation probabilities and rate constants for interconversion of conformers. For the purposes of modeling the behavior of NATMA in a molecular beam after excitation with an IR laser, we use the microcanonical ensemble. The equilibrium occupation probability of a minimum at energy E is

$$P_i^{\text{eq}}(E) = \frac{D_i(E)}{\sum_i D_i(E)}, \quad (1)$$

where $D_i(E)$ is the density of states of minimum i . The rate constant for interconversion of minimum i to minimum j via a transition state \ddagger is given by RRKM theory as

$$k_{ji}^{\ddagger}(E) = \frac{N^{\ddagger}(E)}{hD_i(E)}, \quad (2)$$

where $N^{\ddagger}(E)$ is the sum of states available to the transition state at energy E , excluding the reactive mode. In the present work $D_i(E)$ and $N^{\ddagger}(E)$ were calculated within the harmonic approximation using the Beyer–Swinehart direct count method.¹⁶

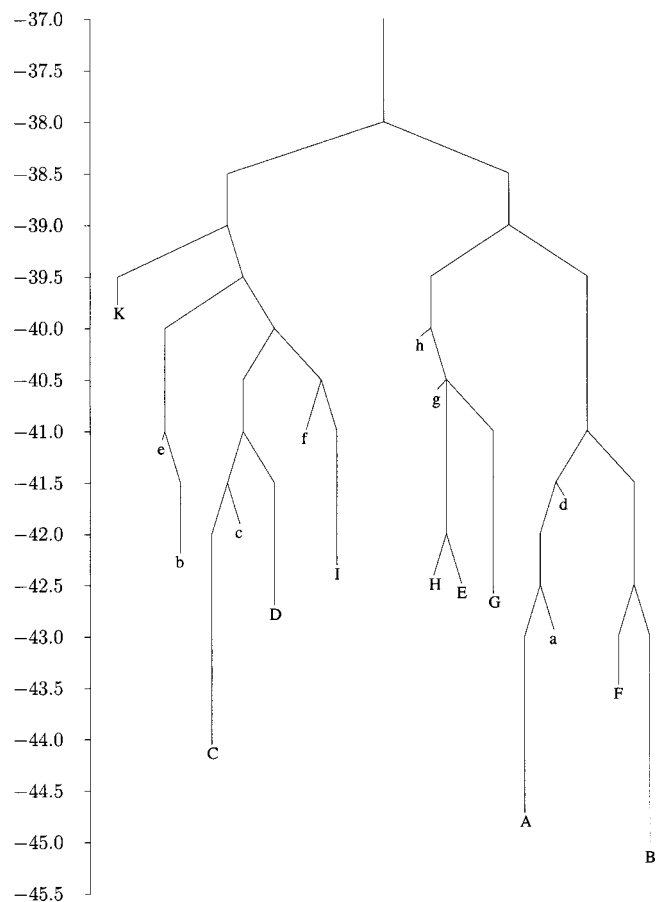


FIG. 3. Disconnectivity graph for the all-*trans* peptide bond region of NATMA calculated using the OPLS-AA force field. The energy is in units of kcal mol⁻¹.

Given the rates $k_{ji}^{\ddagger}(E)$ for every process in the database, it is possible to describe the kinetics of the system via master equation dynamics, with the rate of change of occupation probability of minimum i given by

$$\frac{dP_i(t)}{dt} = \sum_{j \neq i} [k_{ij}(E)P_j(t) - k_{ji}(E)P_i(t)], \quad (3)$$

where $k_{ij} = \sum_{\ddagger} k_{ji}^{\ddagger}(E)$ is a sum over all transition states directly connecting two minima. For a microcanonical system with constant energy E , it is usual to solve Eq. (3) via diagonalization of the symmetrized transition matrix W_{ij}

$$W_{ij} = (P_j^{\text{eq}}/P_i^{\text{eq}})^{1/2} \left[k_{ij} - \delta_{ij} \sum_m k_{mi} \right]. \quad (4)$$

However, the vibrational energy of molecules in the beam will naturally decrease with time, or distance away from the nozzle, as they collide with the buffer gas (argon, in this case). Therefore, it is necessary to integrate Eq. (3) numerically as a function of time, updating the rate constants $k_{ij}(E)$ as the energy changes. The Bulirsch–Stoer algorithm was used for this integration.¹⁷

It is difficult to obtain experimental predictions for the cooling rate, despite work with this aim.^{18,19} We model the decay of the energy theoretically, based on the collision rate of particles in a free jet. Following the analysis by Lubman *et al.*,²⁰ the collision rate, z_{jet} , is given by

$$z_{\text{jet}} = 2^{(1/2)} n_0 \sigma \bar{v}_0 \left[1 + \frac{1}{2} (\gamma - 1) \mathcal{M}_{\text{eff}}^2 \right]^{-1/2 [(\gamma+1)/(\gamma-1)]}, \quad (5)$$

where n_0 is the reservoir density (6.5×10^{19} molecules cm^{-3}), σ is the average collision cross section (estimated at 260 \AA^2), \bar{v}_0 is the mean velocity in the reservoir ($1.5 \times 10^5 \text{ cm s}^{-1}$), γ is the heat capacity ratio (C_p/C_v , taken as the ideal gas value $5/3$), and \mathcal{M}_{eff} is the local Mach number (the ratio of the beam velocity to the local speed of sound). \mathcal{M}_{eff} has been fitted as function of distance from the nozzle, x , by Ashkenas and Sherman:²¹

$$\mathcal{M}_{\text{eff}} = 3.26(x/D - 0.075)^{0.67} - 0.61(x/D - 0.075)^{-0.67}, \quad (6)$$

where D is the diameter of the nozzle. Therefore, given the terminal velocity expansion of the supersonic free jet of helium ($2 \times 10^5 \text{ cm s}^{-1}$), we can use Eqs. (5) and (6) to calculate z_{jet} as a function of time. As our master equation simulation proceeds, every $\Delta t = 1/z_{\text{jet}}$ a collision occurs, and the energy and rate constants are recalculated, along with z_{jet} to determine the subsequent Δt .

The remaining undetermined quantity is the amount of energy lost per collision, ΔE . We approximate

$$\Delta E = \lambda(E - E_{\text{zp}}), \quad (7)$$

where E_{zp} is the zero-point energy of the lowest minimum. This linear dependence appears reasonable based on previous work.¹⁸ This form is anticipated to be least accurate at low energy where the vibrational energy tends to zero, but isomerization will be complete well before these energies are reached. It is important to obtain quantitative experimental data for vibrational energy transfer in large flexible biomolecules, since little can be stated with certainty from a purely theoretical standpoint.

This analysis leaves λ as an undetermined parameter, which controls the cooling rate in our model. The approximate value of λ can be estimated from experimental data, as described below. In Sec. VIA, we present the results for a range of possible λ values.

IV. EXPERIMENTAL COOLING DATA

To estimate the vibrational energy of the molecule after IR excitation, it is necessary to assess the extent of cooling in the early portion of the expansion prior to IR excitation. Figure 4 shows a series of laser-induced fluorescence (LIF) scans taken at various distances from the expansion orifice. Closest to the orifice ($x/D = 0.8$), the expansion is warmest, with little resolved vibronic structure. The other scans in the series show a regular progression toward colder conditions, with the vibronic structure due to the ground-state zero-point level population clearly visible by $x/D = 1.6$, and hot band intensities decreasing smoothly. The IR-induced population transfer spectra were recorded with IR excitation occurring at $x/D = 2.5$. The vibrational temperature can be estimated by comparing the intensities of the $\nu'' = 0 \rightarrow \nu' = 1$ cold band with that for the $\nu'' = 1 \rightarrow \nu' = 0$ hot band, labeled in Fig. 4. In a harmonic analysis, the Franck–Condon factors for these transitions are identical, leading to the following simple relationship between the observed intensity ratio and a vibrational “temperature” in the expansion

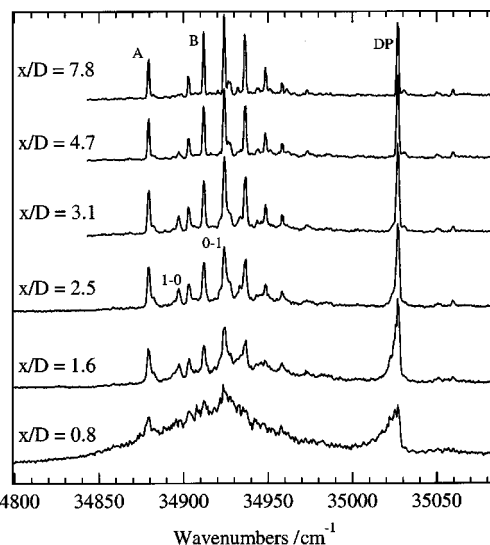


FIG. 4. A series of LIF scans taken at a range of distances from the expansion orifice.

$$\frac{I_{0 \rightarrow 1}}{I_{1 \rightarrow 0}} = \exp(-\Delta E/k_B T). \quad (8)$$

A vibrational temperature of $T_{\text{vib}} = 10\text{--}15 \text{ K}$ is derived from this analysis, consistent with the translational temperature calculated at that point in the expansion. Thus, vibrational cooling seems to be nearly complete at the point of excitation in the experiment.

It is difficult to obtain an experimental estimate of the vibrational cooling rate in the supersonic expansion for a large flexible molecule, such as NATMA. Figure 5 shows a series of experimental IR-UV hole-filling scans taken as a

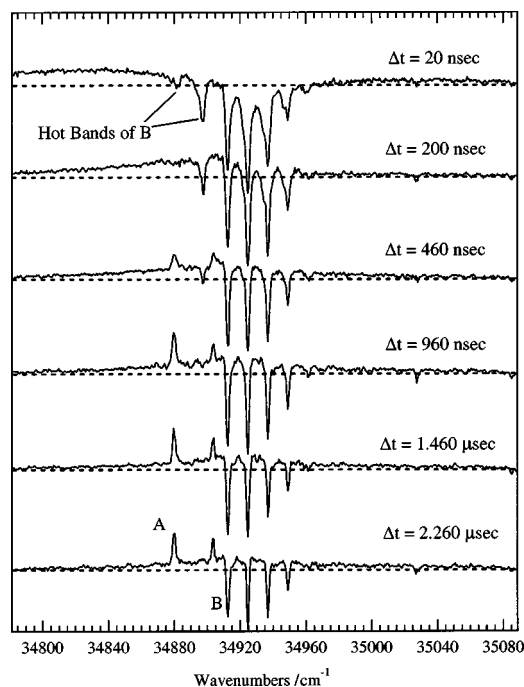


FIG. 5. Experimental IR-UV hole-filling scans taken with different separations (hence, times) between the IR excitation and UV detection points. Taken with the IR laser tuned to a transition of conformer B.

function of distance (and time) between the IR excitation and UV detection points. The scans in Fig. 5 are taken with the IR laser tuned to an IR transition of conformer B at 3454 cm^{-1} . When the IR and UV lasers are overlapped in space, with only 20 ns time delay, the IR-excited molecules are still quite hot, and produce a broad gain that stretches over the entire region surrounding the cold bands in the LIF spectrum. No conformational discrimination is possible at these early times. Analogous scans with longer delays show a narrowing of this broad absorption, but at no time is structure evident in the IR-excited molecules, except when they are cooled into the zero-point levels. This indicates that there is no significant bottleneck in the conformational cooling as the molecules approach the zero-point level. For the series of runs shown in Fig. 5, the cooling into the conformational zero-point levels begins to appear at about 400 ns, and is complete by 900 ns. Isomerization between the three main minima (A, B, and C) will be frozen at much earlier times than this, when the energy falls below the rate-limiting barrier separating them.

V. COOLING SIMULATIONS

The variation of E over time was calculated for values of λ ranging over several orders of magnitude. All runs started from an initial $P_B(0)=1$, in order to model the cooling data shown in Fig. 5. $\lambda \approx 0.003$ gave the best fit (see Fig. 6).

As mentioned in Sec. II, the populations measured downstream in the expansion will be determined by both the equilibrium populations at the initial energy and the cooling rate. To determine the relative size of these effects, we carried out a simulation starting at the expansion orifice. The temperature of the reservoir, 425 K, corresponds to a mean vibrational energy of around 20 kcal mol^{-1} . Therefore, we calculated the equilibrium population distribution at $E = E_{\text{zp}} + 20\text{ kcal mol}^{-1}$, and used this as the initial population distribution in a cooling simulation with this initial energy, with the cooling rate given by $\lambda = 0.003$. The final populations of minima A, B, and C differed from the starting populations by around 10%, indicating that in the absence of IR excitation the energies (and vibrational frequencies in the model used) of the minima are more important in determining the measured final populations than the effect of cooling. The main

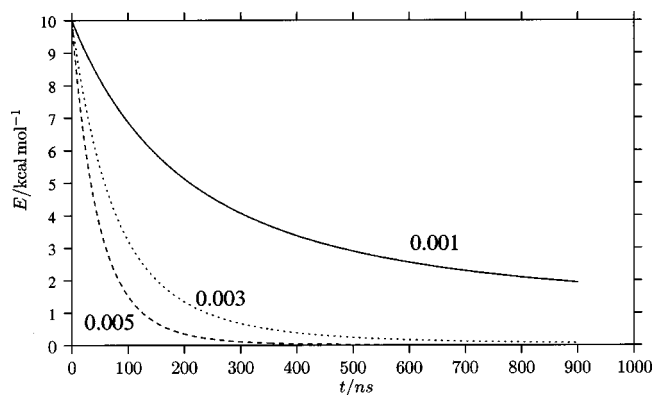


FIG. 6. Variation of energy with time, calculated using the cooling model for different values of λ .

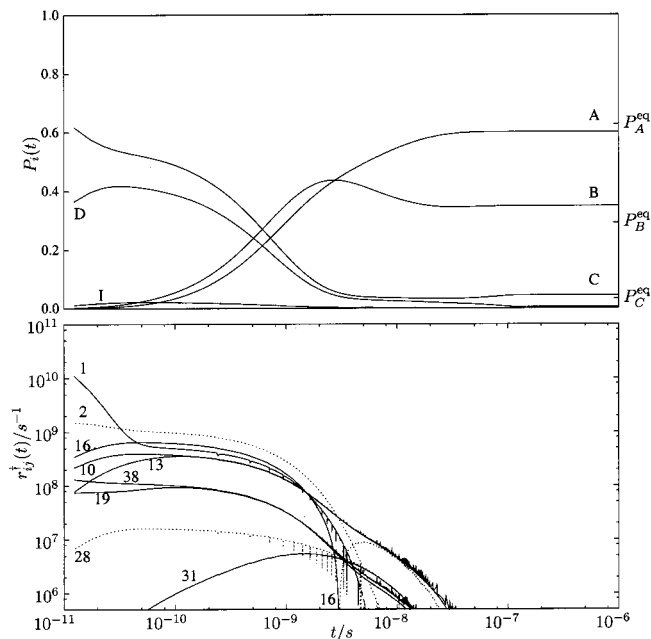


FIG. 7. Results for AMBER, exciting minimum C, with an approximation to the experimental cooling rate, $\lambda = 0.003$. The top plot shows the occupation probabilities for the labeled minima. The bottom plot shows the rate of population transfer, r_{ij}^\ddagger , for the labeled transition states, chosen to be representative of the two significant pathways. r_{ij}^\ddagger is positive for solid lines, negative for dotted lines, where the direction of each transition is as shown in Fig. 9.

difference between the initial and final populations is caused by the movement of population from higher-energy minima into the three dominant low-energy minima A, B, and C.

In the experimental work¹⁴ conformer-specific IR excitation followed by conformer-specific UV spectroscopy allowed the population transfer out of a particular structure to

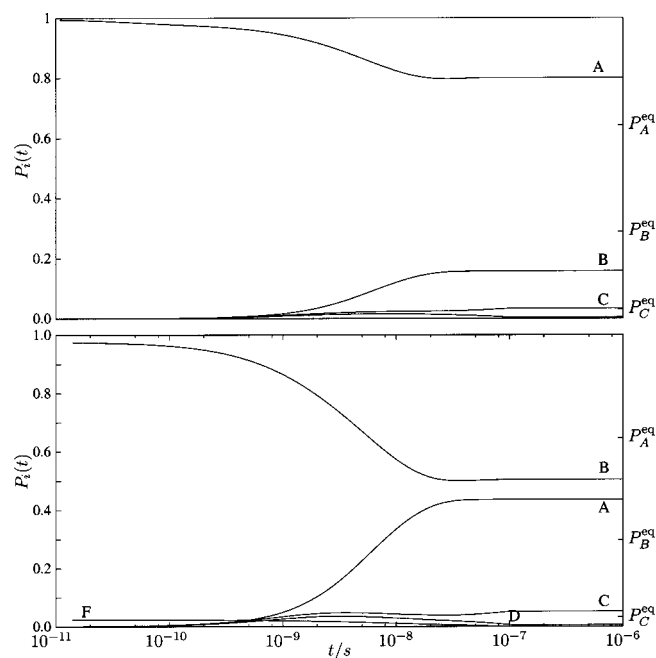


FIG. 8. Results for AMBER, exciting minimum A (top), and minimum B (bottom), with an approximation to the experimental cooling rate, $\lambda = 0.003$.

TABLE I. The final occupation probabilities P_i^f at the end of a $1 \mu\text{s}$ simulation, for the A, B, and C minima. Results are given for two force fields and three different cooling rates, determined by λ [see Eq. (7)]. $i(t=0)$ is the initially excited minimum, $P_i(t=0)=1.0$. $E^{\text{ex}}=10 \text{ kcal mol}^{-1}$ for all simulations. $P_A^f+P_B^f+P_C^f < 1$ because of small populations in the other minima in the system.

λ	$i(t=0)$	AMBER			OPLS-AA		
		P_A^f	P_B^f	P_C^f	P_A^f	P_B^f	P_C^f
0.03	A	0.9580	0.0157	0.0175	0.3348	0.6218	0.0176
	B	0.0527	0.8826	0.0549	0.3347	0.6279	0.0151
	C	0.3454	0.4057	0.2128	0.2295	0.4289	0.2334
0.003	A	0.8011	0.1581	0.0338	0.3099	0.6222	0.0454
	B	0.4360	0.5044	0.0518	0.3105	0.6231	0.0442
	C	0.6004	0.3485	0.0437	0.3099	0.6222	0.0457
0.0003	A	0.6742	0.2818	0.0268	0.3155	0.6086	0.0295
	B	0.6741	0.2808	0.0267	0.3140	0.6118	0.0306
	C	0.6734	0.2780	0.0268	0.3191	0.5991	0.0267

be studied. We model this situation theoretically with each force field, using the subsets of minima depicted in Figs. 2 and 3 and the transition states that connect them. We set the initial population of a single minimum (A, B, or C) $P_i(0)=1$, and all other $P_j(0)=0$. This approach allows direct calculation of the quantum yields discussed in Ref. 1.

From the LIF measurements discussed above, we have determined that virtually all of the vibrational energy is quenched out of the system before the point of IR excitation. Hence, we need only consider the addition of a single photon of IR energy and its subsequent removal by collisions. The energy of the IR photon is around 3500 cm^{-1} , or 10 kcal mol^{-1} . Therefore, we set the initial energy of the system to

$$E_{\text{init}}=E^{\text{ex}}+E_{\text{zero},i}, \quad (9)$$

where the excitation energy $E^{\text{ex}}=10 \text{ kcal mol}^{-1}$ and $E_{\text{zero},i}$ is the zero-point energy of minimum i . We use an energy bin size of $0.0001 \text{ kcal mol}^{-1}$ to discretize the energy levels for the purposes of Beyer–Swinehart counting.

Values of $P_i(t)$ for runs starting from minimum C for the AMBER potential are plotted in Fig. 7, and from A and B in Fig. 8. For comparison, the expected equilibrium values at the initial energy P_i^{eq} are also shown, as calculated by Eq. (1).

The master equation approach allows not only $P_i(t)$ to be plotted for each minimum, but the net flow rate through each transition state, $r_{ij}^\ddagger(t)$ can also be calculated as

$$r_{ij}^\ddagger(t)=P_j(t)k_{ij}^\ddagger(t)-P_i(t)k_{ji}^\ddagger(t). \quad (10)$$

Figure 7 shows that, for $\lambda=0.003$, the cooling is slow enough to allow relaxation to a roughly “equilibrium” distribution, where much of the population finds its way into the global minimum A. However, different distributions are reached in the simulations starting from minima A and B, indicating conformer specificity with this force field and this cooling rate (see Fig. 11 and Table I). The final probability distribution in all cases is reached to within a few percent around 10–100 ns after IR excitation.

A variety of alternative pathways for the transitions between minima A, B, and C are apparent. The significant path-

ways, judged by the size of $r_{ij}^\ddagger(t)$, are represented in Fig. 9. Two routes are shown to be dominant between C and A. The first is via minima D and I, which are significantly populated intermediates at times around 10^{-10} s. The population transfers through transition states 10 and 13 are almost indistinguishable after 10^{-10} s, showing that minimum H, which connects them, is only transiently populated; the steady-state approximation from elementary kinetics is appropriate here. A second path goes through minimum G. Again, the population transfers through transition states 19 and 38 are very close, and the population of G does not build up. The magnitude of the population transfer via this route is less than that for the first pathway, although it is shorter. The total barrier height along these two pathways is roughly the same, but it is more favorable to move over two smaller barriers (transition states 1 and 2) to reach intermediate I than one large barrier (transition state 38) to reach intermediate G.

The analogous simulation data for the OPLS-AA potential is presented in Figs. 10 and 11, again using our best approximation to the experimental cooling rate, $\lambda=0.003$. For this potential, it is clear that the equilibrium distribution is approached for all simulations, starting from minima A, B, or C. The dominant pathways are depicted in Fig. 12.

VI. COMPARISON WITH EXPERIMENT

As noted above, neither force field gives correct predictions of the occupation probabilities when compared to ex-

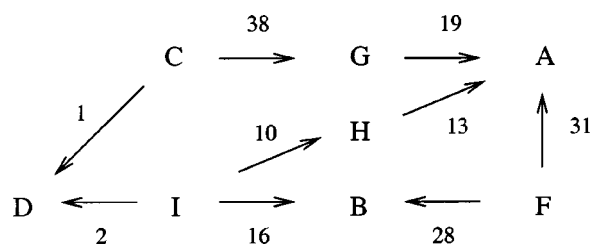


FIG. 9. Significant pathways as calculated using the AMBER potential. Minima are labeled with letters and the numbers above the arrows denote the transition states which link them. The direction of the arrows is arbitrary (generated by the search algorithm) but it is necessary to have a label to describe the direction of the population transfer.

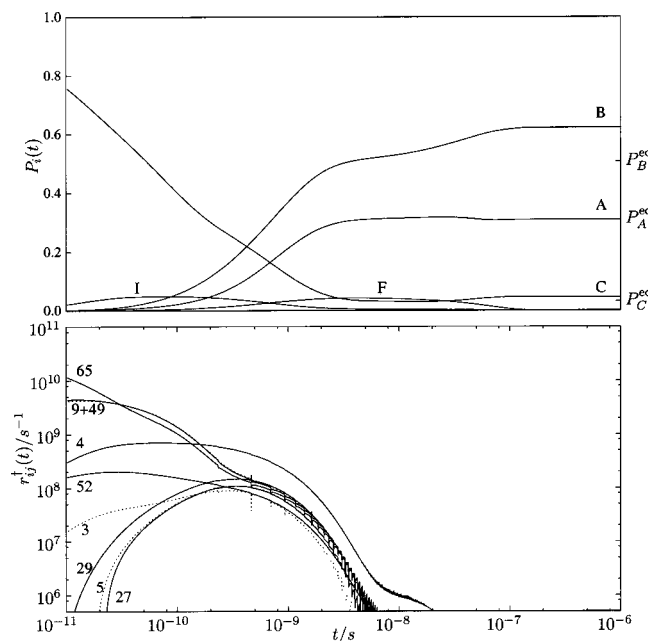


FIG. 10. Results for OPLS-AA, exciting minimum C, with an approximation to the experimental cooling rate, $\lambda=0.003$. The top plot shows the occupation probabilities for labeled minima. P_i^{eq} shows the equilibrium occupation probability of each minimum at the initial energy. The bottom plot shows the rate of population transfer, r_{ij}^{\dagger} , for the labeled transition states, chosen to be representative of the two significant pathways. r_{ij}^{\dagger} is positive for solid lines, negative for dotted lines, where the direction of each transition is as shown in Fig. 12.

periment. It is therefore unlikely that predictions of kinetic properties will be quantitatively accurate. As well as deficiencies in the potentials themselves, the harmonic approximation used to calculate densities of states may lead to inaccuracies, and a better description of anharmonicity (particularly for the torsional degrees of freedom) would be desirable.

However, it is true that some of the general experimental trends are replicated in the AMBER simulations for $\lambda=0.003$. The experimental quantum yields for NATMA [Fig. 12(a) of Ref. 1] show a small conformational specificity with a similar trend; namely, that excitation of a given conformer forms quantum yields biased toward reformation of this same conformer. The simulations indicate that this is because some of the population is trapped near the excited minimum, due to the quenching of vibrational energy at a fast enough rate for the molecules to be unable to cross all the barriers necessary to reach the equilibrium distribution.

In contrast, the final populations in the AMBER simulation starting from an excited C conformer, and in all three OPLS-AA simulations, are relatively unaffected by the collisional cooling and tend toward the equilibrium values. This “slow cooling” limit does not give conformer-specific quantum yields. In order for the RRKM description to account for this aspect of the experimental data, we must be in the moderately “fast cooling” regime, as observed for the AMBER simulations starting from A and B. It is perhaps confusing that the same cooling rate should give different behavior in the AMBER force field depending on the starting minimum. In the simulation with $P_C(0)=1$, the fast initial rate of popula-

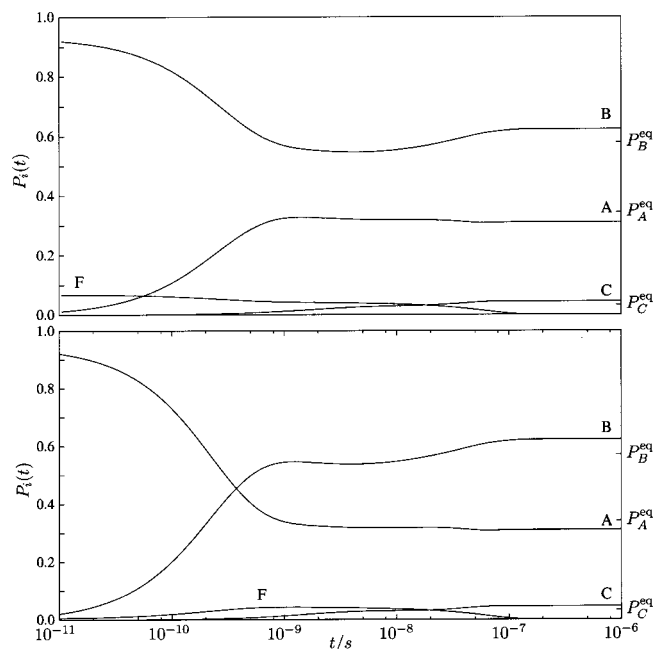


FIG. 11. Results for OPLS-AA, exciting minimum B (top), and minimum A (bottom), with an approximation to the experimental cooling rate, $\lambda=0.003$. P_i^{eq} shows the equilibrium occupation probability of each minimum at the initial energy.

tion transfer into minimum I results in population flow into A and B at roughly equal rates. However, the reverse reactions starting from $P_A(0)=1$ or $P_B(0)=1$ are slower to reach I, and therefore population transfer between A and B is hindered.

A. Alternative cooling rates

Further simulations were carried out varying the cooling rate over two orders of magnitude, in order to investigate a range of possible behavior. The results are given in Table I, and are also represented diagrammatically in the triangular plots of Fig. 13(a). At the slowest cooling rate, $\lambda=0.0003$, both force fields are in the slow cooling regime, where no conformer-specific quantum yields are predicted. At the highest cooling rate, $\lambda=0.03$, both force fields show significant conformer specificity, and the differences between the potentials are highlighted. With the AMBER potential, all runs show significant shifts of population toward the starting minima compared to the distribution reached at lower cooling rate, but the effect is greater for A and B, which are

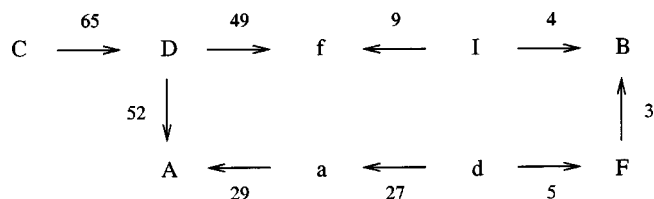


FIG. 12. Significant pathways as calculated with the OPLS-AA potential. Minima are labeled with letters and the numbers above the arrows denote the transition states that link them. The labeling of transition states is not consistent between the AMBER and OPLS-AA potentials, as it was not possible to uniquely identify structures between the two databases, in contrast to the situation with minima.

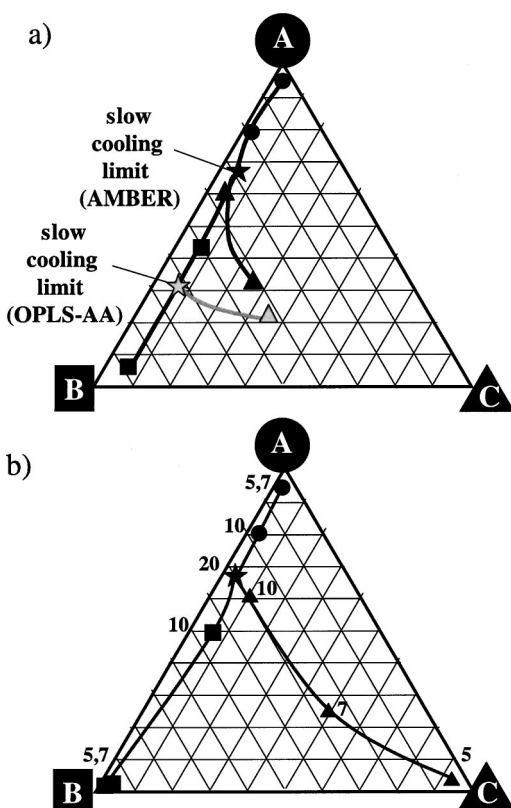


FIG. 13. The quantum yields predicted by the cooling simulations. Simulations starting with initial population in the same minimum are connected by smooth lines. (a) The data for different cooling rates for AMBER, and for OPLS-AA for excitation of C (taken from Table I). The approach to the slow cooling limit as λ decreases is evident. (b) The data for different excitation energies only for AMBER (taken from Table II). The approach to the slow cooling limit as E_{ex} increases is evident.

separated from the rest of the system by higher barriers than C. In OPLS-AA runs at $\lambda=0.03$ starting with $P_A(0)=1$ or $P_B(0)=1$, the population equilibrates between A and B, because of the relatively low barrier between these minima.

Simulations with $P_C(0)=1$, however, show significant trapping of population in C, because the barrier between C and the other two conformers is higher.

Considering the overall variations of behavior with cooling rate, the nonlinear curve observed for the AMBER simulations starting from C is interesting as this indicates that the ratio of A and B generated by exciting C depends on the energy decay of the system.

B. Alternative excitation energies

All of the simulations described above used $E^{\text{ex}}=10 \text{ kcal mol}^{-1}$, corresponding to the fundamental frequency of an NH stretch, which was the region probed experimentally. We also carried out simulations at different excitation energies: $E^{\text{ex}}=5 \text{ kcal mol}^{-1}$ for a carbonyl stretch fundamental, $E^{\text{ex}}=7 \text{ kcal mol}^{-1}$ for an ND stretch fundamental, and $E^{\text{ex}}=20 \text{ kcal mol}^{-1}$ for an NH stretch overtone. The results of these runs are shown in Table II and Fig. 13(b) and constitute predictions for the qualitative behavior which might be seen in future experiments.

It is clear that for the lowest energy, $E^{\text{ex}}=5 \text{ kcal mol}^{-1}$, the population is almost entirely trapped near the starting point. Interestingly, a population of around 10% is predicted for minimum D in the runs starting from C (not shown in Table II). There is a low barrier between these two structures, as shown in Figs. 2 and 3, and so it appears that, at this excitation energy, it is possible to trap population in a minimum which is not observed experimentally in the absence of IR radiation. There must be a delicate balance between cooling rate and excitation energy to allow this to happen, as at higher energies the system will be able to leave D via minimum I, whereas at slower cooling rates, the population would all return to C at longer times.

The results for the highest energy, $E^{\text{ex}}=20 \text{ kcal mol}^{-1}$, are in the opposite slow cooling limit, where all the runs reach the same population regardless of the starting point. The runs at intermediate energies show behavior that lies

TABLE II. The final occupation probabilities P_i^f at the end of a $1 \mu\text{s}$ simulation, for the A, B, and C minima. Results are given for two force fields and four different excitation energies, E^{ex} . $i(t=0)$ is the initially excited minimum, $P_i(t=0)=1.0$, and $\lambda=0.003$ for all simulations.

E^{ex}	$i(t=0)$	AMBER			OPLS-AA		
		P_A^f	P_B^f	P_C^f	P_A^f	P_B^f	P_C^f
5	A	0.9995	0.0000	0.0000	0.8703	0.1276	0.0000
	B	0.0000	0.9995	0.0000	0.0237	0.9757	0.0000
	C	0.0006	0.0006	0.8970	0.0000	0.0000	0.8670
7	A	0.9919	0.0003	0.0034	0.3319	0.6621	0.0004
	B	0.0036	0.9742	0.0195	0.3282	0.6690	0.0000
	C	0.2446	0.2767	0.4290	0.0617	0.1235	0.6718
10	A	0.8011	0.1581	0.0338	0.3099	0.6223	0.0454
	B	0.4360	0.5044	0.0518	0.3105	0.6231	0.0442
	C	0.6004	0.3485	0.0437	0.3097	0.6222	0.0457
20	A	0.6532	0.2989	0.0407	0.3093	0.6238	0.0452
	B	0.6532	0.2989	0.0407	0.3094	0.6238	0.0451
	C	0.6532	0.2989	0.0407	0.3093	0.6239	0.0451

TABLE III. Results for simulations at different excitation energies. Y or N for a given I→J transition denotes whether measurable population (>1%) was obtained in minimum J at the end of a cooling simulation starting with $P_I=1$. $\lambda=0.003$ for all simulations.

E^{ex}	AMBER/OPLS-AA					
	A→B	B→A	A→C	C→A	B→C	C→B
5	N/Y	N/Y	N/N	N/N	N/N	N/N
7	N/Y	N/Y	N/N	Y/Y	N/N	Y/Y
10	Y/Y	Y/Y	Y/Y	Y/Y	Y/Y	Y/Y
20	Y/Y	Y/Y	Y/Y	Y/Y	Y/Y	Y/Y

Note: N=no. Y=yes.

between these two limits, and this is likely to be the most interesting regime for future work.

The results are presented in alternative form in Table III. This format shows whether measurable population transfer between particular pairs of minima is predicted by the simulations when one member of the pair is excited. Again, these results could be compared to future experiments spanning a wider range of well-defined excitation energies. The points in Table III where there is discrepancy between the force fields (the B→A runs) are interesting, as they indicate that the accuracy of potentials can be assessed to some extent. The points where different results are seen for the same pair of minima depending on the direction (A→C, C→A and B→C, C→B) are also interesting, as they allow one to directly determine the relative energy of the two minima. For such variable excitation energy experiments, it would be desirable to use expansion conditions which produced slow cooling, to maximize the extent of isomerization once a particular barrier has been crossed.

VII. CONCLUSIONS

Using empirical force fields and a simple statistical rate theory, we have identified the most important pathways for population transfer between the three main conformers of the NATMA molecule. We have investigated the dependence of the degree of conformational flexibility on the cooling rate in the beam, given a typical initial energy due to excitation of an NH stretch by an IR photon. Even in this simple system, multiple pathways are predicted to be significant which demonstrates the importance of having a global representation of the PES.

The discrepancies between the two empirical force fields AMBER and OPLS-AA are significant, and they appear to predict different behavior at the experimental cooling rate. However, they do give valuable predictions for the low-energy pathways, which could be refined by higher level *ab initio* calculations. For a simple model of the cooling behavior observed experimentally, it appears that the AMBER force field predicts barrier heights between the significant conformers that are consistent with some degree of conformer specificity in the quantum yields, whereas the OPLS-AA potential does not. We have shown that these conclusions are dependent on the cooling rate, and an accurate description of the decay of vibrational energy in the molecular-beam expansion would be desirable to better model these experiments. Simulations carried out at energies corresponding to

different regions of the IR spectrum also show varying behavior, providing an impetus for future experimental work.

Clearly, regardless of the cooling rate, the simple RRKM picture will be unable to account for the mode-specific quantum yields. The experimental results show only a hint of such vibrational mode specificity (i.e., with results falling just outside the error bars separating them) when the two amide NH stretch modes of conformer C were excited. Molecular dynamics simulations, where a particular normal mode is specifically stretched before the system evolves in time, could be used to investigate this, and the results compared with those obtained here to determine the extent of mode selectivity. Techniques applied recently to the anharmonic decay of normal modes in proteins could also provide useful information.²² The results presented here demonstrate that population transfer out of one minimum can occur through many transition states simultaneously (see Figs. 7, 9, 10, and 12). It is plausible that IR excitation of a particular reactive mode could affect the balance of population transfer over these competing transition states, and hence the final quantum yield.

ACKNOWLEDGMENTS

One of the authors (D.A.E.) is grateful to the EPSRC for financial support. Two other authors (T.S.Z. and B.C.D.) gratefully acknowledge the NSF Experimental Physical Chemistry program (CHE0242818) and the Petroleum Research Fund, administered by the American Chemical Society (35988-AC6) for their support of this work.

¹B. C. Dian, A. Longarte, P. R. Winter, and T. S. Zwier, *J. Chem. Phys.* **120**, 133 (2004), preceding paper.

²J. N. Murrell and K. J. Laidler, *J. Chem. Soc. Faraday Trans.* **64**, 371 (1968).

³D. J. Wales, J. P. K. Doye, M. A. Miller, P. N. Mortenson, and T. R. Walsh, *Adv. Chem. Phys.* **115**, 1 (2000).

⁴D. J. Wales, *Energy Landscapes: Applications to Clusters, Biomolecules and Glasses* (Cambridge University Press, Cambridge, UK, 2003).

⁵T. Baer and W. L. Hase, *Unimolecular Reaction Dynamics* (Oxford University Press, New York, 1996).

⁶W. D. Cornell, P. Cieplak, C. I. Bayly, I. R. Gould, K. W. Merz, Jr., D. M. Ferguson, D. C. Spellmeyer, T. Fox, J. W. Caldwell, and P. A. Kollman, *J. Am. Chem. Soc.* **117**, 5179 (1995).

⁷P. Kollman, R. Dixon, W. Cornell, T. Fox, C. Chipot, and A. Pohorille, *Comput. Sim. Biomol. Syst.* **3**, 83 (1997).

⁸W. L. Jorgensen, D. S. Maxwell, and J. Tirado-Rives, *J. Am. Chem. Soc.* **118**, 11225 (1996).

⁹M. A. Miller, J. P. K. Doye, and D. J. Wales, *J. Chem. Phys.* **110**, 328 (1999).

- ¹⁰P. N. Mortenson and D. J. Wales, *J. Chem. Phys.* **114**, 6443 (2001).
- ¹¹C. J. Cerjan and W. H. Miller, *J. Chem. Phys.* **75**, 2800 (1981).
- ¹²D. J. Wales and T. R. Walsh, *J. Chem. Phys.* **105**, 6957 (1996).
- ¹³O. M. Becker and M. Karplus, *J. Chem. Phys.* **106**, 1495 (1997).
- ¹⁴B. C. Dian, A. Longarte, and T. S. Zwier, *Science* **296**, 2369 (2002).
- ¹⁵B. C. Dian, A. Longarte, S. Mercier, D. A. Evans, D. J. Wales, and T. S. Zwier, *J. Chem. Phys.* **117**, 10688 (2002).
- ¹⁶T. Beyer and D. Swinehart, *Commun. ACM* **16**, 379 (1973).
- ¹⁷R. Bulirsch and J. Stoer, *Introduction to Numerical Analysis* (Springer, New York, 1991).
- ¹⁸J. R. Barker, *J. Phys. Chem.* **88**, 11 (1984).
- ¹⁹M. Damm, F. Deckert, and J. Troe, *J. Phys. Chem.* **95**, 2005 (1991).
- ²⁰D. M. Lubman, C. T. Rettner, and R. N. Zare, *J. Phys. Chem.* **86**, 1129 (1982).
- ²¹H. Ashkenas and F. S. Sherman, in *Rarefield Gas Dynamics, 4th Symposium*, edited by J. H. de Leeuw (Academic, New York, 1966), Vol. II.
- ²²X. Yu and D. M. Leitner, *J. Phys. Chem. B* **107**, 1698 (2003).